Research Article

Surface modification of MoS$_2$ nanosheets by single Ni atom for ultrasensitive dopamine detection

Xuejiao Sun[1,2], Cai Chen[2], Can Xiong[2], Congmin Zhang[2], Xusheng Zheng[5], Jin Wang[3], Xiaoping Gao[2,3] (✉), Zhen-Qiang Yu[1] (✉), and Yuen Wu[2,4] (✉)

[1] *College of Chemistry and Environmental Engineering, Institute of Low-dimensional Materials Genome Initiative, Shenzhen University, Shenzhen 518071, China*
[2] *School of Chemistry and Materials Science, University of Science and Technology of China, Hefei 230026, China*
[3] *College of Materials Science and Engineering, Shenzhen University, Shenzhen 518071, China*
[4] *Dalian National Laboratory for Clean Energy, Dalian 116023, China*
[5] *National Synchrotron Radiation Laboratory, University of Science and Technology of China, Hefei 230029, China*

ABSTRACT

Single atom catalysts have been recognized as potential catalysts to fabricate electrochemical biosensors, due to their unexpected catalytic selectivity and activity. Here, we designed and fabricated an ultrasensitive dopamine (DA) sensor based on the flower-like MoS$_2$ embellished with single Ni site catalyst (Ni-MoS$_2$). The limit of detection could achieve 1 pM in phosphate buffer solution (PBS, pH = 7.4), 1 pM in bovine serum (pH = 7.4), and 100 pM in artificial urine (pH = 6.8). The excellent sensing performance was attributed to the Ni single atom axial anchoring on the Mo atom in the MoS$_2$ basal plane with the Ni-S$_3$ structure. Both the experiment and density functional theory (DFT) results certify that this structural feature is more favorable for the adsorption and electron transfer of DA on Ni atoms. The high proportion of Ni active sites on MoS$_2$ basal plane effectively enhanced the intrinsic electronic conductivity and electrochemical activity toward DA. The successful establishment of this sensor gives a new guide to expand the field of single atom catalyst in the application of biosensors.

KEYWORDS

single atom catalysts, MoS$_2$, dopamine (DA) sensor, serum, urine

1   Introduction

Neurological diseases are the current epidemic diseases, such as Depression, Parkinson's disease, Alzheimer's disease, and Schizophrenia, the main cause of these diseases is the abnormal contents of dopamine (DA) [1, 2]. DA is one of vital neurotransmitters, which plays a key role in the functions of central nervous system and cardiovascular system [3, 4]. In addition, DA concentration in urine is the main diagnostic basis for pheochromocytoma and other catecholamine-secreting tumors [5]. Thus, accurate detection of DA *in vivo/in vitro* is very crucial for the routine diagnosis and monitoring. Various technologies have been carried to detect DA concentrations, e.g., high-performance liquid chromatography (HPLC) [6, 7], mass spectrometry [8], and spectrophotometry [9]. However, the high cost, large-scale of instruments requirement and tedious sample pretreatment restrict their further develop. In recent years, the electrochemical biosensors for specific molecule detection have received considerable interest because they are simple, prompt read-out, and cost-effective [10–13]. Regarding DA, it is a highly redox-active molecule, and the reported electrochemical DA sensors with low detection concentration certified that using electrochemical measure to detect DA is an effective method [14–17]. However, most of these reported DA sensors involving precious metal, nucleic acids, aptamers or enzymes, which not only increase the fabrication complexity, but also reduce the stability of their application. Hence, exploring new noble-metal-free electrocatalysts to further improve the sensing performances is still urgently demanded.

Single atom catalysts (SACs) are a new class of electrocatalysts which disperse and anchor isolated metal atoms on solid supports [18–21]. Benefiting from their homogeneously dispersed active sites and high atomic efficiency, SACs have been proposed for using as single-atom nanozymes (SAzymes) to imitate natural enzymes due to high catalytic stability, tunable activity, low cost, and high storage stability [22–28]. Among the SACs for electrochemical reactions, two-dimensional (2D) transition metal dichalcogenide (TMD) MoS$_2$ has been investigated as a rising support material, due to the high surface-to-volume ratio, unique electronic characteristics, and has shown remarkable properties in biomarker detection [14, 29–34]. Considering the special chemical structure of a single tri-atomic MoS$_2$ layer which has a plane of Mo atoms sandwiched between two other planes of S atoms via strong inplane covalent bonding, it is generally accepted that the active centers are the unsaturated coordinative atoms at the surface edges. However, the high proportion of saturated coordinative atoms in the MoS$_2$ surface base planes do not participate in the construction of catalytic active sites which cause it to lose the advantage of high specific surface areas and greatly

limit its electrocatalytic activity. As proved by the theoretical calculation and experimental investigation, surface modification by single atom showed desirable adsorption performance and dramatic enhancement of electronic property due to this anchor form maximize the exposed active site and more conducive to occur catalytic reaction [35, 36].

Considering nickel (Ni) has higher electronegativity and redox couple Ni(II)/Ni(III), it will be more benefited to absorb and oxide DA molecule. Inspired by above analysis, we designed and prepared a flower-like MoS_2 modified by Ni atom (Ni-MoS_2). The DA sensor based on Ni-MoS_2 can ultrasensitively detect DA concentrations in PBS, bovine serum and artificial urine. The limit of detection can achieve 1 pM in phosphate buffer solution (PBS), 1 pM in bovine serum, and 100 pM in artificial urine which is the best sensing behavior comparing with ever reported single atom and nanoparticles based materials [14, 16, 29, 30, 37]. The experimental results and theoretical calculation proved that the excellent sensing performance is attributed to the isolate Ni atom which located on the top of Mo in the MoS_2 basal plane. The high proportion of active sites could effectively improve the catalyze active and efficiency to DA oxidation. The excelled DA sensing performances in serum and artificial urine suggest the sensor has potential to practical application. The successful establishment of this sensor points out a new direction for designing high active SAzymes in further research.

2　Experimental

2.1　Synthesis of nickel complex

Briefly, 0.156 g 4,4-pyridine was dissolved in 10 mL tetrahydrofuran, then 0.248 g Ni(OAc)$_2$·4H$_2$O was added into the solution with continuous stirring for 24 h at room temperature. The resultant precipitate was centrifuged and then washed for several times with pentane. Finally, the obtained Ni complex was dried in a vacuum oven for further use.

2.2　Synthesis of Ni-MoS_2

As shown in Fig. 1(a), the Ni-MoS_2 was synthesized following the two-steps below: firstly, using the same hydrothermal process as reported previously to synthesize the flower-like MoS_2 [38]. Typically, 0.07 g Na$_2$MoO$_4$·H$_2$O and 0.06 g L-cysteine were dissolved in 15 mL water with stirring for 15 min to form a clear solution. Then another 15 mL water was added into the solution. The as-obtained mixtures were transferred into 50 mL Teflon-seal autoclaves and heated at 200 °C oven for 18 h. The autoclaves were cooled down naturally to room temperature. The products were collected by filtration and washed by water for three times and ethanol for two times. Finally, the powders were dried in an oven at 50 °C overnight. Secondly, a certain mass of MoS_2 were dispersed in a mixture of deionized (DI) water (5 mL) and ethanol (5 mL), followed by addition of 10 mg prepared Nickel complex. Then the homogeneous solution was heated under 80 °C for recrystallization. The crystalline powder product was moved in a crucible with a cap and transformed to a tube furnace. Then the precursors were heated with a ramping rate of 5 °C·min^{-1} to 900 °C and kept for 2 h under protection of Ar.

2.3　Preparation of the electrode modified with Ni-MoS_2

The fabricated process of working electrode was as follows. Firstly, the bare glassy carbon electrode (GCE) was polished to mirror smoothness with 0.05 μm alumina slurry and residual alumina was removed by ultrasonicating the electrode triply in distilled water for 2 min, then dried in air at ambient temperature. Then 5 mg·mL^{-1} Ni-MoS_2 suspension was prepared using isopropanol as

the dispersing agent by ultrasonic treatment for 2 h. Subsequently, 10 μL composite dispersion was dropped on the surface of bare GCE and dried in air at ambient temperature to prepare Ni-MoS_2/GCE.

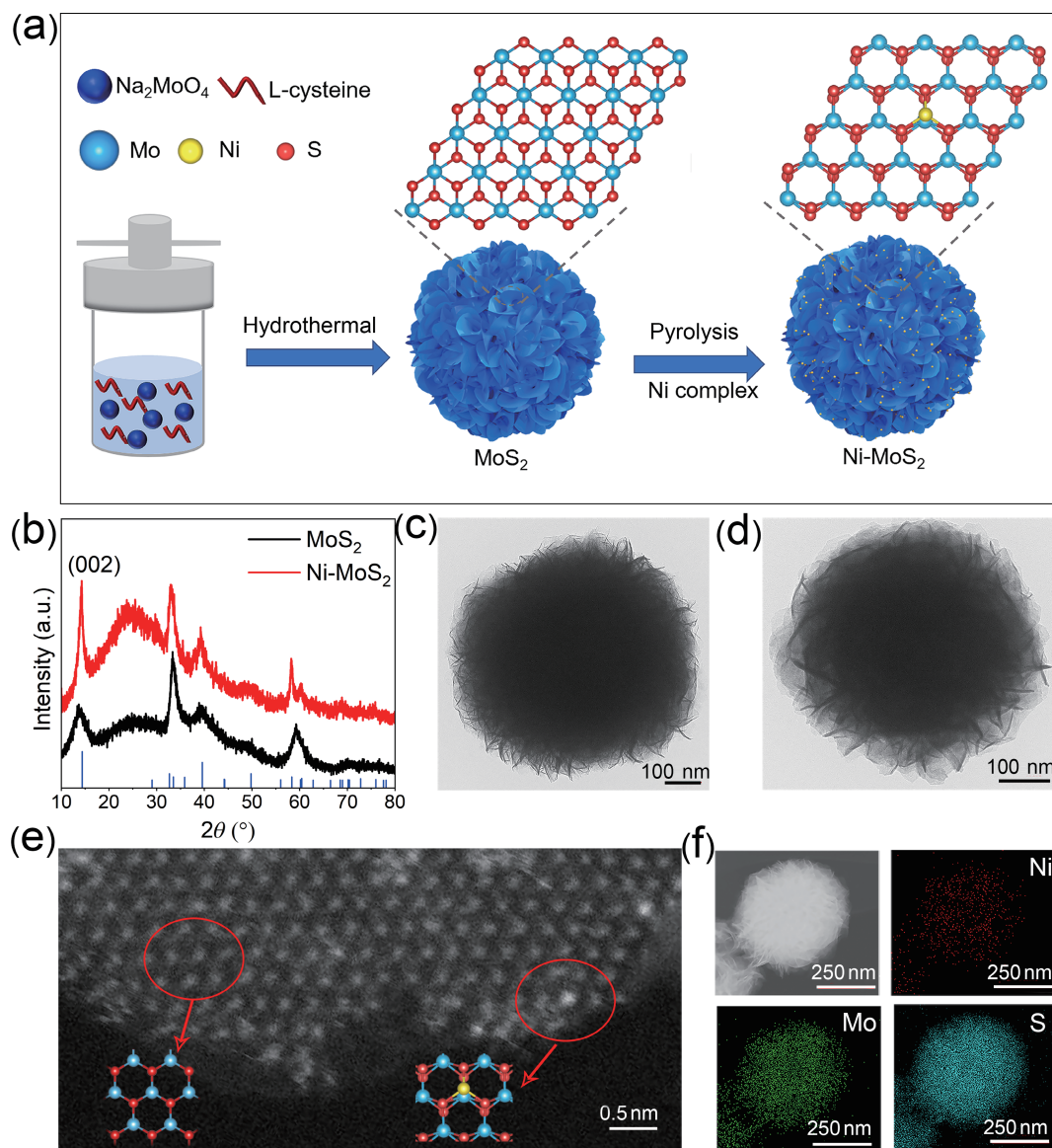### 2.4　Electrochemical characterization

Cyclic voltammetry (CV), electrochemical impedance spectroscopy (EIS), differential pulse voltammetry (DPV), and chronoamperometry were employed as electrochemical techniques which were conducted with a CHI 760E electrochemical workstation. The conventional three-electrode system contains modified GCE (3 mm in diameter), Ag/AgCl electrode (Sat. KCl), and platinum as working electrode, reference electrode, and counter electrode, respectively. The supporting electrolyte was using 0.1 M PBS (pH = 7.4). CV measurements were taken from –0.2 to 0.5 V at scan rates ranging from 10 to 100 mV·s^{-1}, DPV was taken at scan rate of 8 mV·s^{-1}; sampling width of 0.2 s; pulse amplitude of 50 mV; and pulse period of 0.5 s. The EIS measurement was applied in a wide frequency range from 10 MHz to 1 Hz with an amplitude of 5 mV to the working electrode in PBS (1 mM DA, pH = 7.4).

3　Results and discussion

3.1　Characterization

The MoS_2 and Ni-MoS_2 were prepared as illustrated in Fig. 1(a). The X-ray diffraction (XRD) patterns are shown in Fig. 1(b), the spectra of Ni-MoS_2 and MoS_2 are similar as that of 2H-MoS_2 (PDF# 77-1716), and no impurity peaks were found. In addition, there are no peaks of Ni crystals, suggesting the Ni is atomically dispersed. As for the 2θ peak of (002), the notable peak of Ni-MoS_2 suggests the relatively thick layered structure [39]. As shown in the images of transmission electron microscopy (TEM) (Figs. 1(c) and 1(d)) and scanning electron microscope (SEM) (Fig. S1 in the Electronic Supplementary Material (ESM)), the as synthesized MoS_2 and Ni-MoS_2 showed a flower-like nanosheet appearance, and the nanosheet of Ni-MoS_2 is thicker than MoS_2, which is consistent with XRD result. Moreover, no crystals were observed in Ni-MoS_2 nanosheets. In order to further intuitively and clearly observe the microscopic Ni atomic arrangement, the high-angle annular dark-field scanning transmission electron microscopy (HAADF-STEM) was carried out. The Fig. 1(e) shows the MoS_2 accord with simulated pattern of 2H phase (inset in Fig. 1(e)). The high-resolution TEM (HRTEM) image of initial MoS_2 is shown in Fig. S1(c) in the ESM, which can be observed that the phase of MoS_2 changed after Ni modified. According to the results reported by Cui et al. [35], the singly dispersed brighter spots in random place are probably the Ni atoms located on the top of Mo, the simulation model is shown in Fig. 1(e). The energy dispersive spectroscopy (EDS) mappings of Ni-MoS_2 are shown in Fig. 1(f), which displayed the homogeneous distribution of Ni, Mo, and S elements.

To verify the coordination environment of atomic Ni dispersed on the MoS_2, the extended X-ray absorption fine structure (EXAFS) and X-ray absorption near-edge structure (XANES) spectroscopies were performed. As the Ni K-edge XANES spectra shown (Fig. 2(a)), the energy of Ni-MoS_2 is higher than that of Ni foil, and close to that of NiS, demonstrating the average valence state of Ni is around +2 [40, 41]. In the field-emission EXAFS (FT-EXAFS) spectra (Fig. 2(b)), a single strong shell at 1.7 Å in *R*-space was found, which assigned to the Ni–S bond. The typical Ni–Ni peak was not detected in the spectra, suggesting the Ni atoms in these samples retain atomic dispersion. According to the fitting curves (Fig. 2(c)) and fitting parameters (Table S1 in the ESM), the

Figure 1 Scheme illustration and characterization. (a) Scheme of the formation of Ni-MoS$_2$, (b) XRD patterns of MoS$_2$ and Ni-MoS$_2$, (c) TEM image of MoS$_2$, (d) TEM image of Ni-MoS$_2$, (e) HAADF-STEM image of Ni-MoS$_2$ (inset: simulation model of 2H-MoS$_2$ and Ni-MoS$_2$), and (f) EDS mappings of Ni, Mo, and S element.

isolated Ni single atom fits well with the Ni-S$_3$ structure. As shown in Fig. 2(h) and Fig. S2(a) in the ESM, the wavelet transforms (WT) of Ni K-edge EXAFS oscillations and K-edge EXAFS k$^2\chi$ functions visually showed Ni–S coordination for Ni-MoS$_2$.
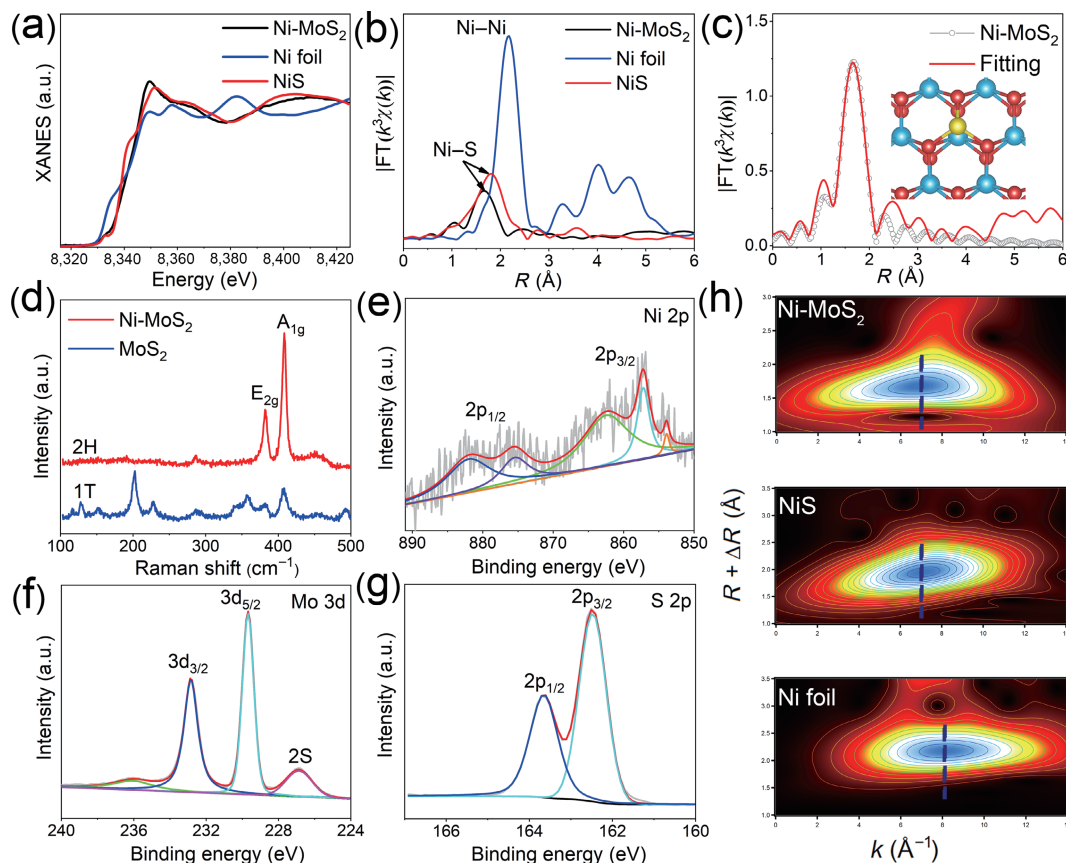
Additionally, the phase and chemical state can also be identified by the Raman and X-ray photoelectron spectroscopy (XPS) measurements. The most important difference between the metallic 1T-MoS$_2$ and semiconducting 2H-MoS$_2$ lies in the symmetricity of the S in their crystal structures, as shown in Fig. 1(a). These crystal structural variations in 1T-MoS$_2$ and 2H-MoS$_2$ can be easily distinguished from their Raman spectra [42]. As shown in Fig. 2(d), differing from typical 2H monolayer with two main vibration peaks of E$_{2g}$ and A$_{1g}$, several characteristic Raman modes in MoS$_2$ were observed at 127, 152, 203, 228, 286, and 357 cm^{-1}, which is well coincided with 1T structure [43]. In addition, the E$_{2g}$ peak as characteristic peak of 2H-MoS$_2$ shows little signal in corresponding position, further verifying high phase purity. As for the Raman modes of Ni-MoS$_2$, the character peaks of 2H phase were observed, suggesting the phase changed to 2H-MoS$_2$ after Ni single atom introducing. Elemental ingredients analyzed by XPS were performed to confirm chemical states of elements and the phase state, thus the spectra of Ni 2p, Mo 3d, and S 2p of Ni-MoS$_2$ are shown in Figs. 2(e)–2(g). In the Ni 2p$_{2/3}$

spectrum, only one single peak located at 857.1 eV was observed, which can be assigned to Ni^{2+}, and the peak located at 853.7 eV can be recognized as the Ni–S–Mo bonding [44]. The peak of Ni–Ni was no found which further providing the evidence for single-atom dispersion of Ni in Ni-MoS$_2$ [45]. The noticeable signal noise is attributed to the high dispersion and low concentration of Ni atoms, as shown in Table S2 in the ESM. Comparing Mo 3d and S 2p of Ni-MoS$_2$ regions with that of MoS$_2$ (Figs. S2(b) and S2(c) in the ESM), additional peaks can be seen in MoS$_2$, revealing the formation of 1T phase. The peaks in Ni-MoS$_2$ are similar with the typical 2H-MoS$_2$ peaks, proving that 1T-MoS$_2$ transfer to 2H-MoS$_2$. The reason is due to the Ni atoms loading on the MoS$_2$ surface by pyrolysis, however, the metallic 1T-MoS$_2$ is not stable which tends to transfer to stable 2H phase in high temperature.
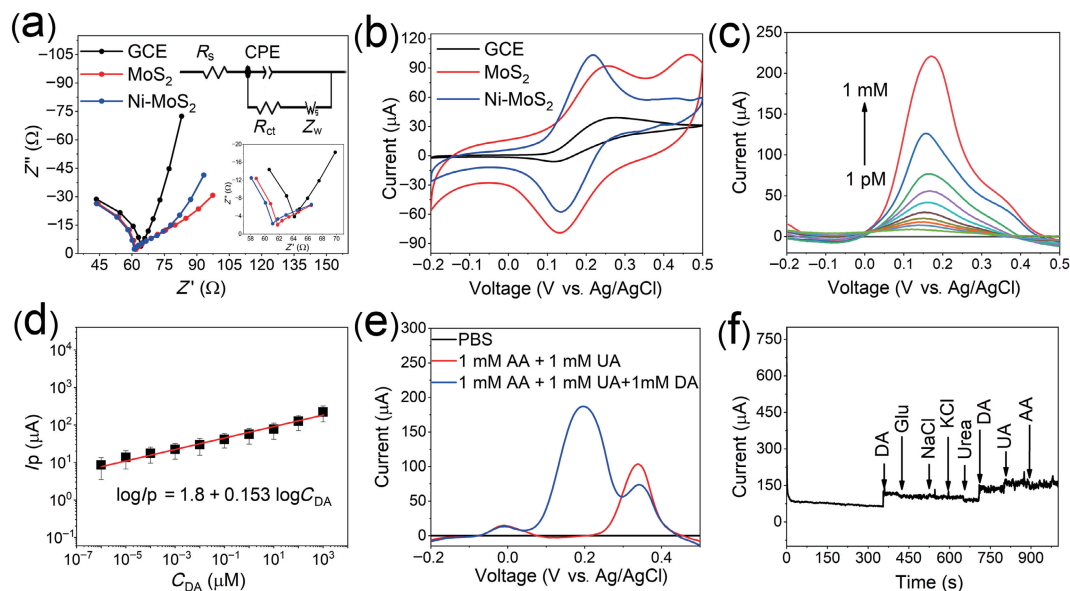
3.2 Electrochemical characterization

To characterize and compare the electrochemical activation of three fabricated electrodes, the EIS and CV were applied to record the performance of bare GCE, MoS$_2$/GCE, and Ni-MoS$_2$/GCE to Fe(CN)$_6^{3-}$/Fe(CN)$_6^{4-}$ and 1 mM DA. Figure 3(a) showed the Nyquist plots for three electrodes in 0.1 M KCl containing 1 mM Fe(CN)$_6^{3-}$/Fe(CN)$_6^{4-}$, and the standard Randle's equivalent circuit

Figure 2 Characterization of MoS$_2$ and Ni-MoS$_2$. (a) The Ni K-edge XANES spectra. (b) FT- EXAFS spectra of Ni K-edge in Ni-MoS$_2$. (c) EXAFS fitting curves of Ni K-edge in Ni-MoS$_2$ (inset: atomic structure model of Ni-MoS$_2$). (d) Ramam image. The XPS spectra of Ni-MoS$_2$ (e) Ni 2p, (f) Mo 3d, and (g) S 2p. (h) The WT for the k^3-weighted EXAFS signals of Ni-MoS$_2$.

Figure 3 Electrochemical characterization and sensing performance. (a) The EIS results for three electrodes in 0.1 M KCl containing 1 mM Fe(CN)$_6^{3-}$/Fe(CN)$_6^{4-}$, and the standard Randle's equivalent circuit model. (b) The CV curves of three electrodes toward 1 mM DA in PBS. (c) DPV data of different DA concentrations in PBS using Ni-MoS$_2$/GCE. (d) Calibration curves current peak versus C_{DA} derived from the DPV data. (e) DPV curves for 1 mM AA+1 mM UA, and 1 mM AA+1 mM UA+1 mM DA. (f) Amperometric responses of the Ni-MoS$_2$/GCE for the addition of 1 mM DA, 1 mM glucose, 1 mM NaCl, 1 mM KCl, 1 mM urea, 1 mM UA, and 1 mM AA in PBS.

model, where R_S, CPE, R_{ct}, and Z_W represent the uncompensated solution resistance, a constant phase element, charge transfer resistance, and Warburgh impedance, respectively. Comparatively, according to the fitting EIS spectra, the Ni-MoS$_2$/GCE and MoS$_2$/GCE exhibited lower electronic transfer resistance than bare GCE. The Ni-MoS$_2$/GCE showed more favorable kinetics than MoS$_2$/GCE, suggesting that loading Ni atoms on 2H-MoS$_2$ plane

can vastly enhance its intrinsic conductivity, even better than the metallic 1T-MoS$_2$.

The electrochemical responses of bare GCE, MoS$_2$/GCE, and Ni-MoS$_2$/GCE toward 1 mM DA in PBS were further investigated. As the CV results shown in Fig. 3(b), a pair of well-defined redox peaks were observed at all of electrodes. The oxidation peak current of Ni-MoS$_2$/GCE (91.9 μA) is much higher than that of

GCE (25.6 μA) and MoS$_2$/GCE (43.4 μA). This result could be attributed to the enhanced catalytic activity of Ni atoms. The effect of scan rate for 1 mM DA in PBS was studied by CV at Ni-MoS$_2$/GCE. In the Fig. S3(a) in the ESM, the redox peak current increases with increasing of scan rate in the range of 10–100 mV·s^{-1}. The relationships between the anodic and cathode peak current (I_{pa} and I_{pc}) and the square root of the scan rates ($v^{1/2}$) are shown in Fig. S3(b) in the ESM. A good linearity was obtained with the linear regression equations I_{pa} (μA) = 17$v^{1/2}$ − 22, (R^2 = 0.987) and I_{pc} (μA) = 40 − 12$v^{1/2}$, (R^2 = 0.971). These results indicate that the redox of DA at Ni-MoS$_2$/GCE is diffusion-controlled process.

3.3 Sensing performance

The DPV technology was employed to determine different DA concentrations at Ni-MoS$_2$/GCE in PBS, as shown in Fig. 3(c). A well-defined anodic peak at 0.15 V was selected as a signal relative to the concentrations. The peak currents varied with the DA concentration ranging from 1 pM to 1 mM, moreover, the peak currents and DA concentrations were followed a good proportional relationship with a correlation coefficient of 0.99 as shown in Fig. 3(d). The limit of detection (LOD) of Ni-MoS$_2$/GCE is 1 pM which is the lowest DA sensors than most of reports previously, as shown in Table 1. This result can attribute to that the oxidation of DA to dopaminoquinone (DAQ) is relative to two electrons transfer, the low electronic transfer resistance and high electrochemical DA catalytic activation of Ni-MoS$_2$ are advantage to DA sensing. The Ni atoms are considered as the catalytic sites for DA oxidation, which are more capable of absorbing and activating DA molecules than Mo atom.

Selectivity is another essential performance to evaluate the quality of biosensors. In the extracellular fluids of the central nervous system and serum, ascorbic acid (AA) and uric acid (UA) are the main interfering substances. To evaluate the selectivity of this sensor, we detected DA in the presence of AA and UA in PBS by the DPV method. As shown in Fig. 3(e), the mixture solution containing 1 mM AA and 1 mM UA was tested. Firstly, the peaks of AA and UA were observed at −0.01 and 0.34 V, respectively. While the peak of UA oxidation declined with increasing 1 mM DA in the mixture solution, demonstrating that Ni-MoS$_2$/GCE is substantially more responsive to DA than UA. Although the peak of AA was almost no change, the peak current was much less than DA. Moreover, the peak position was completely separated, thus the interference of AA can be ignored. In the presence of other interfering substances which exist in serum and urine, the anti-interference capability of the Ni-MoS$_2$/GCE electrode to DA was evaluated by chronoamperometry method (Fig. 3(f)). No response current changes can be seen after adding 1 mM glucose, 1 mM NaCl, 1 mM KCl, 1 mM urea, 1 mM AA, and 1 mM UA. A large current change was observed with adding 1 mM DA, indicating that the sensor presents a high selectivity to DA molecules.

As studied previously, the repeatability and store stability of the electrode are also two important factors, because that it is hard to avoid extrinsic variations during fabrication and application processes. The repeatability was evaluated by the DPV responses of five independent modified electrodes under the same PBS containing 1 mM DA, the peak currents are shown in Fig. S4(a) in the ESM, the relative standard deviation (RSD) was calculated to 3.2%. These results can conclude that the sensor has acceptable repeatability. For the environmentally stable in air, the electrode performance toward 1 mM DA was tested every day, as shown in Fig. S4(b) in the ESM. There is only 11.4% loss of its initial response after 7 days, suggesting the good ambient stability.

For the potential application to quantify the DA concentration in the physiological conditions, we explored the sensing performances of the Ni-MoS$_2$/GCE by standard addition method in several bovine serum samples. The serum samples were diluted 100 times using PBS prior to determination. The results, as shown in Table 2, indicate that the fabricated sensor can detect DA concentration as low as 1 pM in serum. As known, the DA could be detected in another biologically complex sample, like urine. The abnormal presence of DA in urine was also associated with various diseases, thus we prepared artificial urine according to the

Table 1 Comparison of the fabricated DA sensors reported in the literatures

Electrode	Linear range (μM)	Detection limit (μM)	References
PEDOT-LSG	1−150	0.33	[46]
RGO-Pd-NPs	1−150	0.23	[47]
CC-NPC	2−200	0.60	[48]
GO-GCE	1−15	0.27	[49]
K$_2$Fe$_4$O$_7$ -GCE	1−40, 40−140	0.22	[12]
SWCNTs-GCE	0.5−100	0.19	[50]
WO$_3$NPs/GCE	0.1−50, 50−600	0.024	[51]
AuNPs@MoS$_2$	0.05−30	0.05	[52]
MoS$_2$/rGO/AuNPs	0.3−198.3	0.11	[53]
Mn-MoS$_2$/PGS	0.00005−50	0.00005	[30]
Ni-MoS$_2$/GCE	0.000001−1,000	0.000001	This work

Table 2 Determination of DA in bovine serum

Sample	Added	Found	Recovery (%)	RSD (%)
1	10 μM	10.20 μM	102.0	1.03
2	1 μM	0.97 μM	97.00	1.25
3	100 nM	105 nM	105.0	1.97
4	1 nM	1.03 nM	103.0	2.15
5	1 pM	1.02 pM	99.98	2.63

reported previously [54], as list in Table S3 in the ESM, and tested the detectability of the sensor toward different DA concentrations. Due to the pH of urine is partial acid than serum and PBS, thus we measure the DPV responses in artificial urine (pH = 6.8). And the plots with linear relationship are shown in Fig. S5(a) in the ESM. The LOD in artificial urine is 100 pM and a good proportion relationship of I_p and C_{DA} was shown in Fig. S5(b) in the ESM. The favourable sensing performance of this sensor in serum and artificial urine well proved the potential application ability.

3.4 Density functional theory (DFT) calculations

The interactions between materials and DA were investigated by DFT calculations. The constructed models were established according to the EXAFS fitting data, where one Ni atom was coordinated with three S atoms (Fig. S6(c) in the ESM). As a contrast, the interaction of the 1T-MoS$_2$ and 2H-MoS$_2$ with DA was also studied (Figs. S6(a) and S6(b) in the ESM), it is worth noting that the 1T-MoS$_2$ is unstable, it is facility to occur the phase transformation during the adsorption of DA, so the 1T-MoS$_2$ substrate was fixed for the DA adsorption. In the simulation, the adsorption energies of 1T-MoS$_2$, 2H-MoS$_2$, and Ni-MoS$_2$ towards DA are shown in Fig. 4(a). The top view and side view are shown in Fig. S6 in the ESM. As shown, DA absorption on the Ni atom has much stronger binding energy (−1.58 eV) than that on the in-plane of 1T-MoS$_2$ (−0.78 eV) and 2H-MoS$_2$ (−0.74 eV), indicating that DA was inclined to adsorb on the Ni atom. Electron density difference analysis demonstrates the enriched electron density in the region between Ni and DA, indicating the superiority of Ni sites for DA activation (Figs. 4(b)–4(d)). As for the selectivity, the structure models of AA and UA adsorbed on Ni-MoS$_2$ were constructed and the top and side view are shown in Fig. S7 in the ESM. As shown in Fig. 4(a), the adsorption energies of AA and UA were −1.28 and −1.36 eV, respectively, which are lower than that of DA absorbed on the Ni atom. These results further verified the above experimental results.
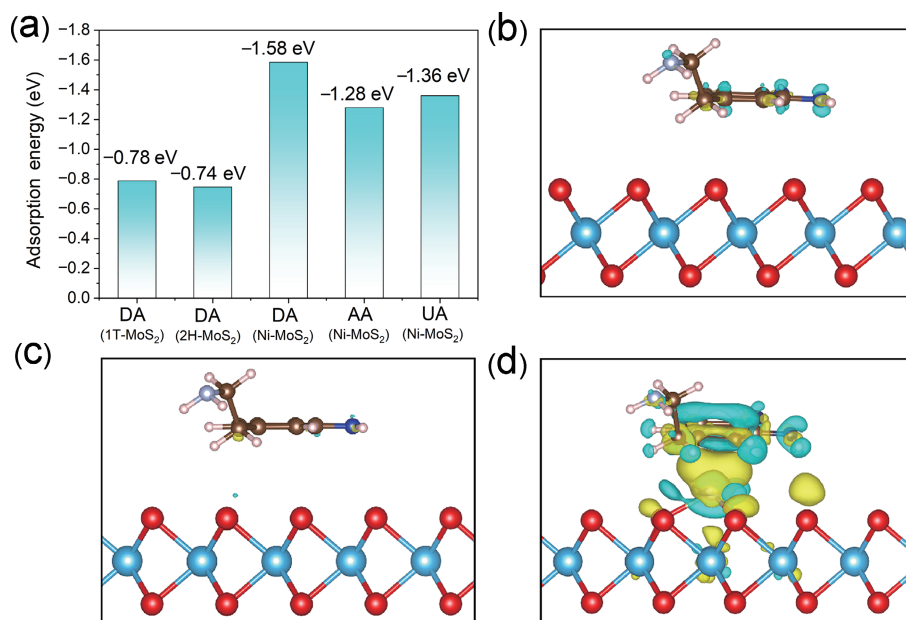
4 Conclusions

In this work, we designed and prepared Ni single-atom decorated flower-like MoS$_2$, and the XRD, TEM, Raman, and XPS results proved that the MoS$_2$ intrinsic phase changed from 1T to 2H with the increasing of layer thickness in high temperature. The HADDF-HRTEM and EXAFS results showed single Ni atom coordinated with three adjacent sulfur atoms, and located at the site directly above the center Mo atom. The Ni atoms significantly improved the electrochemical signals and catalysis activity toward DA. The fabricated sensor based on Ni-MoS$_2$ displayed a wide linear concentration range with a LOD of 1 pM in PBS. In addition, the sensor also showed excellent selectivity and stability. The results of DA detection in serum and artificial urine are acceptable. The enhanced sensing performances are attributed to the low electronic transfer resistance and high electrochemical catalytic activation of Ni-MoS$_2$, and the high active surface is advantaged to DA oxidation. The DFT results further prove that the Ni atoms are more sensitive and selective to adsorb and oxide DA. This single atom catalysis can be assembled into test strips to test the DA content in blood and urine for further practical application. This study provides a new approach for progressing single atom catalysis to a new filed of electrochemical biosensors for neuropathic disease monitoring.

Figure 4 DFT calculations. (a) The adsorption energy of DA on 1T-MoS$_2$, 2H-MoS$_2$, and Ni-MoS$_2$. (b)–(d) Electron density difference analysis of DA adsorbed on 1T-MoS$_2$, 2H-MoS$_2$, and Ni-MoS$_2$, where the isosurface value is set to be 0.001 e·Å^{-3}. (The brown sphere represents C atom, blue represents O atom, gray represents N atom, pink represents H atom, yellow represents electron accumulation, and cyan denotes electron depletion, respectively).

Beijing Synchrotron Radiation Facility (BSRF), BL14W1 in Shanghai Synchrotron Radiation Facility (SSRF), and BL10B and BL11U in National Synchrotron Radiation Laboratory (NSRL) for the help in characterizations. The DFT calculations in this work were performed at the Supercomputing Center of the University of Science and Technology of China. Special thanks go to the Instrumental Analysis Center of Shenzhen University (Lihu Campus).

References

[1] Laviolette, S. R. Dopamine modulation of emotional processing in cortical and subcortical neural circuits: Evidence for a final common pathway in schizophrenia? *Schizophr. Bull.* **2007**, *33*, 971–981.

[2] Piggott, M. A.; Marshall, E. F.; Thomas, N.; Lloyd, S.; Court, J. A.; Jaros, E.; Burn, D.; Johnson, M.; Perry, R. H.; McKeith, I. G. et al. Striatal dopaminergic markers in dementia with Lewy bodies, Alzheimer's and Parkinson's diseases: Rostrocaudal distribution. *Brain* **1999**, *122*, 1449–1468.

[3] Bird, E. D.; Spokes, E. G. S.; Iversen, L. L. Increased dopamine concentration in limbic areas of brain from patients dying with schizophrenia. *Brain* **1979**, *102*, 347–360.

[4] Sharman, D. F. The catabolism of catecholamines: Recent studies. *Br. Med. Bull.* **1973**, *29*, 110–115.

[5] Shukla, R. P.; Aroosh, M.; Matzafi, A.; Ben-Yoav, H. Partially functional electrode modifications for rapid detection of dopamine in urine. *Adv. Funct. Mater.* **2021**, *31*, 2004146.

[6] El-Beqqali, A.; Kussak, A.; Abdel-Rehim, M. Determination of dopamine and serotonin in human urine samples utilizing microextraction online with liquid chromatography/electrospray tandem mass spectrometry. *J. Sep. Sci.* **2007**, *30*, 421–424.

[7] Hows, M. E. P.; Organ, A. J.; Murray, S.; Dawson, L. A.; Foxton, R.; Heidbreder, C.; Hughes, Z. A.; Lacroix, L.; Shah, A. J. High-performance liquid chromatography/tandem mass spectrometry assay for the rapid high sensitivity measurement of basal acetylcholine from microdialysates. *J. Neurosci. Methods* **2002**, *121*, 33–39.

[8] Huang, F.; Li, J.; Shi, H. L.; Wang, T. T.; Muhtar, W.; Du, M.; Zhang, B. B.; Wu, H.; Yang, L.; Hu, Z. B. et al. Simultaneous quantification of seven hippocampal neurotransmitters in depression mice by LC-MS/MS. *J. Neurosci. Methods* **2014**, *229*, 8–14.

[9] Wang, J.; Hu, Y. Y.; Zhou, Q.; Hu, L. Z.; Fu, W. S.; Wang, Y. Peroxidase-like activity of metal-organic framework [Cu(PDA)(DMF)] and its application for colorimetric detection of dopamine. *ACS Appl. Mater. Interfaces* **2019**, *11*, 44466–44473.

[10] Cesewski, E.; Johnson, B. N. Electrochemical biosensors for pathogen detection. *Biosens. Bioelectron.* **2020**, *159*, 112214.

[11] Qing, X.; Wang, Y. D.; Zhang, Y.; Ding, X. C.; Zhong, W. B.; Wang, D.; Wang, W.; Liu, Q. Z.; Liu, K.; Li, M. F. et al. Wearable fiber-based organic electrochemical transistors as a platform for highly sensitive dopamine monitoring. *ACS Appl. Mater. Interfaces* **2019**, *11*, 13105–13113.

[12] Sun, X. J.; Zhang, L.; Zhang, X. H.; Liu, X. X.; Jian, J.; Kong, D. C.; Zeng, D. C.; Yuan, H. M.; Feng, S. H. Electrochemical dopamine sensor based on superionic conducting potassium ferrite. *Biosens. Bioelectron.* **2020**, *153*, 112045.

[13] Zhong, R. B.; Tang, Q.; Wang, S. P.; Zhang, H. B.; Zhang, F.; Xiao, M. S.; Man, T. T.; Qu, X. M.; Li, L.; Zhang, W. J. et al. Self-assembly of enzyme-like nanofibrous G-molecular hydrogel for printed flexible electrochemical sensors. *Adv. Mater.* **2018**, *30*, 1706887.

[14] Bai, Y. C.; Zhang, W. D. Highly sensitive and selective determination of dopamine in the presence of ascorbic acid using Pt@Au/MWNTs modified electrode. *Electroanalysis* **2010**, *22*, 237–243.

[15] Patriarchi, T.; Mohebi, A.; Sun, J. Q.; Marley, A.; Liang, R. Q.; Dong, C. Y.; Puhger, K.; Mizuno, G. O.; Davis, C. M.; Wiltgen, B. et al. An expanded palette of dopamine sensors for multiplex imaging *in vivo*. *Nat. Methods* **2020**, *17*, 1147–1155.

[16] Qian, T.; Yu, C. F.; Zhou, X.; Wu, S. S.; Shen, J. Au nanoparticles decorated polypyrrole/reduced graphene oxide hybrid sheets for ultrasensitive dopamine detection. *Sens. Actuat. B:Chem.* **2014**, *193*, 759–763.

[17] Wen, M. Z.; Xing, Y.; Liu, G. Y.; Hou, S. L.; Hou, S. F. Electrochemical sensor based on Ti$_3$C$_2$ membrane doped with UIO-66-NH$_2$ for dopamine. *Mikrochim. Acta* **2022**, *189*, 141.

[18] Ji, S. F.; Chen, Y. J.; Wang, X. L.; Zhang, Z. D.; Wang, D. S.; Li, Y. D. Chemical synthesis of single atomic site catalysts. *Chem. Rev.* **2020**, *120*, 11900–11955.

[19] Zhou, H.; Zhao, Y. F.; Xu, J.; Sun, H. R.; Li, Z. J.; Liu, W.; Yuan, T. W.; Liu, W.; Wang, X. Q.; Cheong, W. C. et al. Recover the activity of sintered supported catalysts by nitrogen-doped carbon atomization. *Nat. Commun.* **2020**, *11*, 335.

[20] Zhuang, Z. C.; Li, Y. H.; Yu, R. H.; Xia, L. X.; Yang, J. R.; Lang, Z. Q.; Zhu, J. X.; Huang, J. Z.; Wang, J. O.; Wang, Y. et al. Reversely trapping atoms from a perovskite surface for high-performance and durable fuel cell cathodes. *Nat. Catal.* **2022**, *5*, 300–310.

[21] Li, R. Z.; Wang, D. S. Understanding the structure-performance relationship of active sites at atomic scale. *Nano Res.* **2022**, *15*, 6888–6923.

[22] Huang, L.; Chen, J. X.; Gan, L. F.; Wang, J.; Dong, S. J. Single-atom nanozymes. *Sci. Adv.* **2019**, *5*, eaav5490.

[23] Ji, S. F.; Jiang, B.; Hao, H. G.; Chen, Y. J.; Dong, J. C.; Mao, Y.; Zhang, Z. D.; Gao, R.; Chen, W. X.; Zhang, R. F. et al. Matching the kinetics of natural enzymes with a single-atom iron nanozyme. *Nat. Catal.* **2021**, *4*, 407–417.

[24] Zhang, X. L.; Li, G. L.; Chen, G.; Wu, D.; Zhou, X. X.; Wu, Y. N. Single-atom nanozymes: A rising star for biosensing and biomedicine. *Coord. Chem. Rev.* **2020**, *418*, 213376.

[25] Wang, S.; Hu, Z. F.; Wei, Q. L.; Zhang, H. M.; Tang, W. N.; Sun, Y. Q.; Duan, H. Q.; Dai, Z. C.; Liu, Q. Y.; Zheng, X. W. Diatomic active sites nanozymes: Enhanced peroxidase-like activity for dopamine and intracellular H$_2$O$_2$ detection. *Nano Res.* **2022**, *15*, 4266–4273.

[26] Zhang, Q. Q.; Guan, J. Q. Applications of single-atom catalysts. *Nano Res.* **2021**, *15*, 38–70.

[27] Zhao, Y.; Yu, Y. P.; Gao, F.; Wang, Z. Y.; Chen, W. X.; Chen, C.; Yang, J.; Yao, Y. C.; Du, J. Y.; Zhao, C. et al. A highly accessible copper single-atom catalyst for wound antibacterial application. *Nano Res.* **2021**, *14*, 4808–4813.

[28] Zhu, D. M.; Ling, R. Y.; Chen, H.; Lyu, M.; Qian, H. S.; Wu, K. L.; Li, G. X.; Wang, X. W. Biomimetic copper single-atom nanozyme system for self-enhanced nanocatalytic tumor therapy. *Nano Res.* **2022**, *15*, 7320–7328.

[29] Barua, S.; Dutta, H. S.; Gogoi, S.; Devi, R.; Khan, R. Nanostructured MoS$_2$-based advanced biosensors: A review. *ACS Appl. Nano Mater.* **2018**, *1*, 2–25.

[30] Lei, Y.; Butler, D.; Lucking, M. C.; Zhang, F.; Xia, T. N.; Fujisawa, K.; Granzier-Nakajima, T.; Cruz-Silva, R.; Endo, M.; Terrones, H. et al. Single-atom doping of MoS$_2$ with manganese enables ultrasensitive detection of dopamine: Experimental and computational approach. *Sci. Adv.* **2020**, *6*, eabc4250.

[31] Liu, R.; Fei, H. L.; Ye, G. L. Recent advances in single metal atom-doped MoS$_2$ as catalysts for hydrogen evolution reaction. *Tungsten* **2020**, *2*, 147–161.

[32] Wang, L. L.; Liu, X.; Luo, J. M.; Duan, X. D.; Crittenden, J.; Liu, C. B.; Zhang, S. Q.; Pei, Y.; Zeng, Y. X.; Duan, X. F. Self-optimization of the active site of molybdenum disulfide by an irreversible phase transition during photocatalytic hydrogen evolution. *Angew. Chem., Int. Ed.* **2017**, *56*, 7610–7614.

[33] Wu, S. X.; Zeng, Z. Y.; He, Q. Y.; Wang, Z. J.; Wang, S. J.; Du, Y. P.; Yin, Z. Y.; Sun, X. P.; Chen, W.; Zhang, H. Electrochemically reduced single-layer MoS$_2$ nanosheets: Characterization, properties, and sensing applications. *Small* **2012**, *8*, 2264–2270.

[34] Liu, M. M.; Li, H. X.; Liu, S. J.; Wang, L. L.; Xie, L. B.; Zhuang, Z.

C.; Sun, C.; Wang, J.; Tang, M.; Sun, S. J. et al. Tailoring activation sites of metastable distorted 1T'-phase MoS$_2$ by Ni doping for enhanced hydrogen evolution. *Nano Res.* **2022**, *15*, 5946–5952.

[35] Qi, K.; Cui, X. Q.; Gu, L.; Yu, S. S.; Fan, X. F.; Luo, M. C.; Xu, S.; Li, N. B.; Zheng, L. R.; Zhang, Q. H. et al. Single-atom cobalt array bound to distorted 1T MoS$_2$ with ensemble effect for hydrogen evolution catalysis. *Nat. Commun.* **2019**, *10*, 5231.

[36] Su, H. Y.; Chen, L. L.; Chen, Y. Z.; Si, R.; Wu, Y. T.; Wu, X. N.; Geng, Z. G.; Zhang, W. H.; Zeng, J. Single atoms of iron on MoS$_2$ nanosheets for N$_2$ electroreduction into ammonia. *Angew. Chem., Int. Ed.* **2020**, *59*, 20411–20416.

[37] Xie, X. L.; Wang, D. P.; Guo, C. X.; Liu, Y. H.; Rao, Q. H.; Lou, F. M.; Li, Q. N.; Dong, Y. Q.; Li, Q. F.; Yang, H. B. et al. Single-atom ruthenium biomimetic enzyme for simultaneous electrochemical detection of dopamine and uric acid. *Anal. Chem.* **2021**, *93*, 4916–4923.

[38] Xin, X.; Song, Y. R.; Guo, S. H.; Zhang, Y. Z.; Wang, B. L.; Wang, Y. J.; Li, X. H. One-step synthesis of P-doped MoS$_2$ for efficient photocatalytic hydrogen production. *J. Alloys Compd.* **2020**, *829*, 154635.

[39] Gao, X. Q.; Qi, J.; Wan, S. H.; Zhang, W.; Wang, Q.; Cao, R. Conductive molybdenum sulfide for efficient electrocatalytic hydrogen evolution. *Small* **2018**, *14*, 1803361.

[40] Chen, J. Y.; Li, H.; Fan, C.; Meng, Q. W.; Tang, Y. W.; Qiu, X. Y.; Fu, G. T.; Ma, T. Y. Dual single-atomic Ni-N$_4$ and Fe-N$_4$ sites constructing Janus hollow graphene for selective oxygen electrocatalysis. *Adv. Mater.* **2020**, *32*, 2003134.

[41] Ge, J. M.; Zhang, D. B.; Qin, Y.; Dou, T.; Jiang, M. H.; Zhang, F. Z.; Lei, X. D. Dual-metallic single Ru and Ni atoms decoration of MoS$_2$ for high-efficiency hydrogen production. *Appl. Catal. B: Environ.* **2021**, *298*, 120557.

[42] Jian, J.; Li, H.; Sun, X. J.; Kong, D. C.; Zhang, X. H.; Zhang, L.; Yuan, H. M.; Feng, S. H. 1T-2H Cr$_x$-MoS$_2$ ultrathin nanosheets for durable and enhanced hydrogen evolution reaction. *ACS Sustainable Chem. Eng.* **2019**, *7*, 7227–7232.

[43] Peng, J.; Liu, Y. H.; Luo, X.; Wu, J. J.; Lin, Y.; Guo, Y. Q.; Zhao, J. Y.; Wu, X. J.; Wu, C. Z.; Xie, Y. High phase purity of large-sized 1T'-MoS$_2$ monolayers with 2D superconductivity. *Adv. Mater.* **2019**, *31*, 1900568.

[44] Luo, R. C.; Luo, M.; Wang, Z. Q.; Liu, P.; Song, S. X.; Wang, X. D.; Chen, M. W. The atomic origin of nickel-doping-induced catalytic enhancement in MoS$_2$ for electrochemical hydrogen production. *Nanoscale* **2019**, *11*, 7123–7128.

[45] Wang, Q.; Zhao, Z. L.; Dong, S.; He, D. S.; Lawrence, M. J.; Han, S. B.; Cai, C.; Xiang, S. H.; Rodriguez, P.; Xiang, B. et al. Design of active nickel single-atom decorated MoS$_2$ as a pH-universal catalyst for hydrogen evolution reaction. *Nano Energy* **2018**, *53*, 458–467.

[46] Xu, G. Y.; Jarjes, Z. A.; Desprez, V.; Kilmartin, P. A.; Travas-Sejdic, J. Sensitive, selective, disposable electrochemical dopamine sensor based on PEDOT-modified laser scribed graphene. *Biosens. Bioelectron.* **2018**, *107*, 184–191.

[47] Palanisamy, S.; Ku, S. H.; Chen, S. M. Dopamine sensor based on a glassy carbon electrode modified with a reduced graphene oxide and palladium nanoparticles composite. *Microchim. Acta* **2013**, *180*, 1037–1042.

[48] Zhao, D. Y.; Yu, G. L.; Tian, K. L.; Xu, C. X. A highly sensitive and stable electrochemical sensor for simultaneous detection towards ascorbic acid, dopamine, and uric acid based on the hierarchical nanoporous PtTi alloy. *Biosens. Bioelectron.* **2016**, *82*, 119–126.

[49] Gao, F.; Cai, X. L.; Wang, X.; Gao, C.; Liu, S. L.; Gao, F.; Wang, Q. X. Highly sensitive and selective detection of dopamine in the presence of ascorbic acid at graphene oxide modified electrode. *Sens. Actuat. B:Chem.* **2013**, *186*, 380–387.

[50] Yang, Y.; Li, M. X.; Zhu, Z. W. A novel electrochemical sensor based on carbon nanotubes array for selective detection of dopamine or uric acid. *Talanta* **2019**, *201*, 295–300.

[51] Anithaa, A. C.; Lavanya, N.; Asokan, K.; Sekar, C. WO$_3$ nanoparticles based direct electrochemical dopamine sensor in the presence of ascorbic acid. *Electrochim. Acta* **2015**, *167*, 294–302.

[52] Sun, H. F.; Chao, J.; Zuo, X. L.; Su, S.; Liu, X. F.; Yuwen, L. H.; Fan, C. H.; Wang, L. H. Gold nanoparticle-decorated MoS$_2$ nanosheets for simultaneous detection of ascorbic acid, dopamine and uric acid. *RSC Adv.* **2014**, *4*, 27625–27629.

[53] Zhao, Y. N.; Zhou, J.; Jia, Z. M.; Huo, D. Q.; Liu, Q. Y.; Zhong, D. Q.; Hu, Y.; Yang, M.; Bian, M. H.; Hou, C. J. *In-situ* growth of gold nanoparticles on a 3D-network consisting of a MoS$_2$/rGO nanocomposite for simultaneous voltammetric determination of ascorbic acid, dopamine and uric acid.. *Mikrochim. Acta* **2019**, *186*, 92.

[54] Pietrzyńska, M.; Voelkel, A. Stability of simulated body fluids such as blood plasma, artificial urine and artificial saliva. *Microchem. J.* **2017**, *134*, 197–201.